

1 Interpretation of Vector Electric Field Measurements 2 of Bursty Langmuir Waves in the Cusp

M. P. Dombrowski¹, J. LaBelle¹, D. E. Rowland², R. F. Pfaff², and
C. A. Kletzing³

M. P. Dombrowski, Department of Physics and Astronomy, Dartmouth College, Room 315, 6127 Wilder Laboratory, Hanover, NH 03755, USA. (mpd@dartmouth.edu)

J. LaBelle, Department of Physics and Astronomy, Dartmouth College, Room 336, 6127 Wilder Laboratory, Hanover, NH 03755, USA. (jlabelle@aristotle.dartmouth.edu)

D. E. Rowland, Space Weather Laboratory, Heliophysics Science Division, NASA Goddard Space Flight Center, Greenbelt, MD, USA.

R. F. Pfaff, Space Weather Laboratory, Heliophysics Science Division, NASA Goddard Space Flight Center, Greenbelt, MD, USA.

C. A. Kletzing, Department of Physics and Astronomy, University of Iowa, Room 502, Van Allen Hall, Iowa City, IA 52242, USA. (cak@delta.physics.uiowa.edu)

¹Department of Physics and Astronomy,

3 **Abstract.** An analysis of auroral Langmuir waves in the cusp observed
4 by two HF electric-field instruments on the TRICE high-flyer sounding rocket
5 shows many examples of Langmuir wave bursts modulated at approximately
6 10 kHz. Previous studies have explained these and similar observations as
7 the result of beating between waves with very close frequencies near the Lang-
8 muir cutoff, resulting from either wave-wave interactions or independent lin-
9 ear excitations. The unique 3-D data set provided by the NASA Goddard
10 Space Flight Center TAEFWD instrument shows that up to 25% of wave-
11 forms selected from the most intense bursts exhibit anisotropic modulations,
12 i.e. the beat nulls and peaks are not aligned in time across the three perpen-
13 dicular electric-field components. Modulations of this type arise when super-
14 posed wave normal modes possess differing polarizations, and simulations
15 using wave modes calculated with the J-WHAMP numerical dispersion code
16 show that waves with differing polarizations can exist in conditions like those
17 observed by TRICE-High, and that superpositions of such waves can pro-

Dartmouth College, Hanover, NH, USA.

²Space Weather Laboratory, Heliophysics
Science Division, NASA Goddard Space
Flight Center, Greenbelt, MD, USA.

³Department of Physics and Astronomy,
University of Iowa, Iowa City, IA, USA.

18 duce anisotropic modulation. Fourier analysis of the 3-D waveform data sug-
19 gests that both linear and elliptically-polarized waves are present near the
20 Langmuir cutoff at these times. These observations illustrate how 3-D mea-
21 surements can give valuable insight into the nature of wave interactions in
22 the auroral plasma environment.

1. Introduction

23 The electron-beam plasma interaction in the Earth's auroral ionosphere produces a va-
24 riety of plasma waves, and Langmuir waves are among the most intense and ubiquitous
25 of these. Sounding rocket observations of Langmuir waves in both the night- and dayside
26 aurora show similar features: the waves occur in bursts with durations from ms to hun-
27 dreds of ms and amplitudes from mV/m to hundreds of mV/m [*Boehm, 1987; McFadden*
28 *et al., 1986; McAdams et al., 1999*]. The bursts are modulated at frequencies ranging
29 from < 1 kHz to > 50 kHz [*Ergun et al., 1991; Bonnell et al., 1997; LaBelle et al., 2010*].
30 Satellite data confirm many of these observations [*Beghin et al., 1981; Stasiewicz et al.,*
31 *1996; Kintner et al., 1996*].

32 The modulation of auroral Langmuir waves has been attributed to mixing of multiple
33 wave normal modes on the Langmuir surface. Indeed, spectra of the modulated waves
34 show multiple peaks, extremely well resolved in recent experiments [*LaBelle et al., 2010*].
35 Linear [*Maggs, 1976; Newman et al., 1994b*] and nonlinear [*Newman et al., 1994a*] theory
36 suggests that the auroral electron beam can excite a range of Langmuir modes, including
37 modes at oblique angles. There is some controversy, however, about the origin of the
38 interfering waves. Most papers in the literature favor wave-wave interaction, whereby a
39 primary Langmuir wave, directly excited by the beam, decays into a second Langmuir wave
40 and a whistler or ion sound wave, with the observed modulation resulting from the beating
41 of the two Langmuir waves [*Bonnell et al., 1997; Stasiewicz et al., 1996; Lizunov et al.,*
42 *2001; Khotyaintsev et al., 2001*]. The absence of evidence for the low frequency wave in
43 many observations is explained by strong wave damping. An alternative hypothesis holds

44 that two different Langmuir waves directly excited by linear processes at slightly different
45 locations in the strongly inhomogeneous plasma mix to make the observed modulations
46 [*LaBelle et al.*, 2010]. In this case, no third wave would be expected to occur.

47 A major shortcoming of previous rocket experiments is the absence of three-dimensional
48 field data at high frequencies. Recently, however, the availability of higher rocket telemetry
49 rates and the increasing power of onboard processing enabled the TRICE sounding rocket
50 mission to include such measurements. In principle, having all three components of the
51 electric field provides more information about the wave modes comprising the modulated
52 Langmuir waves. Section 2 below describes the TRICE instrumentation; Section 3 shows
53 measured three-dimensional waveforms; and Section 4 presents a model for explaining
54 observed effects.

2. Instrumentation

55 The Twin Rockets to Investigate Cusp Electrodynamics (TRICE) were launched 10 Dec
56 2007 at 0900 and 0902 UT, from Andoya, Norway, reaching apogees of 1145 km and 750
57 km. The rockets were launched into an active cusp, with poleward-moving auroral forms
58 monitored with all-sky cameras and multiple radars. K_p was relatively low, with a value
59 of two. The payload's spin axis was kept aligned with the background magnetic field, B_0 ,
60 by a NASA Attitude Control System (ACS), which activated at specific times during the
61 flight, and was otherwise turned off to minimize interference. Each rocket carried electron
62 and ion detectors, swept Langmuir probes, low-frequency to DC electric-field probes,
63 magnetometers, and two complementary high-frequency electric-field instruments: the
64 Dartmouth High-Frequency Electric-field experiment (HFE), and the NASA GSFC Tri-

65 Axial Electric-Field Wave Detector (TAEFWD). Figure 1 shows the probe configuration
66 for the HF instruments.

67 The Dartmouth HFE detects the potential difference between two 2.5 cm spherical
68 probes, separated by 30 cm along the payload’s spin axis. This ΔV signal provides an
69 estimate of the the axial component of the electric-field, which is mainly parallel to the
70 ambient magnetic field, given the payload alignment. The signal is band-pass filtered to
71 the 100 kHz to 5 MHz band, and regulated by an Automatic Gain Control (AGC) system
72 to enhance the dynamic range. The AGC control signal is sampled onboard at 20 kHz
73 and telemetered with other digital data. The regulated HF signal directly modulates a 5
74 MHz-bandwidth S-band transmitter, and the resulting waveform is continuously digitized
75 at the ground telemetry station at 10 MHz, with 12-bit resolution. This instrument is
76 the latest iteration of a design which has flown on numerous rocket campaigns in both
77 E_{\parallel} and E_{\perp} configurations, including HIBAR [*Samara et al.*, 2004], PHAZE II [*McAdams*
78 *et al.*, 1998], SIERRA, RACE [*Samara and LaBelle*, 2006], ACES [*Kaeppler et al.*, 2011],
79 and CHARM II [*Kletzing et al.*, 2012].

80 The GSFC TAEFWD measures ΔV between three pairs of 2.5 cm probes separated
81 by 47.5 cm (X axis) or 45.5 cm (Y and Z axes) along three orthogonal axes: an X axis
82 perpendicular to the payload spin axis, and Y and Z axes 45 degrees off of the spin axis,
83 in a plane perpendicular to X. After filtering to a 4 MHz bandwidth (-3dB bandwidth),
84 the onboard TAEFWD receiver synchronously digitizes these three signals, as well as the
85 Dartmouth HFE output signal, at 8 MSps, in 2048-sample snapshots, with the snapshots
86 being gathered at 15.625 Hz cadence, yielding a 0.4% duty cycle and a 1.92 MBps data

87 stream (after packing into 10-bit words). The sensitivity level was approximately 80
88 $\mu\text{V}/\text{m}$, suitable for measurement of large-amplitude Langmuir waves in the cusp region.

89 Both payloads were affected by various payload systems failures and instrumental
90 anomalies, resulting in the complete loss of particle data and interference in other data,
91 including the generation of extraneous signals; however, the DC magnetometer and both
92 HF electric-field experiments obtained good data over most of the flight. The HFE data
93 in particular resulted in a study of cusp Langmuir waves [*LaBelle et al.*, 2010].

94 Between ACS activations, imperfections in the payload weight distribution caused the
95 payload to begin to misalign from B_0 , with the spin axis precessing around B_0 by an
96 increasing angle—an effect known as ‘coning’. On TRICE, unlike most flights, this effect
97 could not be compensated for because the payload attitude data provided by the ACS
98 package was of low quality due to interference. Over the interval important to this study,
99 the payload magnetometer showed a variance in B_0 from perfect spin-axis alignment of
100 5-10%, implying a similar variance in the components of the electric field parallel and
101 perpendicular to B_0 .

3. Observations

102 As shown by *LaBelle et al.* [2010], the TRICE high-flyer passed through auroral activity
103 that generated significant high-frequency waves. Figure 2a is a 0 to 2.5 MHz spectrogram
104 of HFE data from almost the entire flight (100 to 1100 seconds after launch). General
105 features of this plot include: a 100 kHz rolloff due to the band-pass filter; vertical bands
106 which are caused by the AGC system raising and lowering the noise floor when the total
107 signal amplitude changes; additional, cadenced vertical bands at 60 s intervals, which are
108 instrument-calibration signals injected into the receiver; and multiple horizontal bands,

109 the strongest of which are due to interference from payload systems. Malfunctions in the
110 particle instruments also resulted in periods of strong interference 100–400 kHz, e.g. at
111 710–845 s, 865–880 s, and 900–920 s. These broadly resemble natural auroral hiss, but
112 have been attributed to arcing in high-voltage components [*LaBelle et al.*, 2010].

113 Besides the artificial features, the full-flight spectrogram shows signals of natural origin,
114 such as wave cutoffs of the type which have proven effective for measuring electron plasma
115 density on previous flights. Two such upper cutoffs can be seen near the beginning of this
116 flight: a higher-frequency cutoff that emerges from diffuse noise near 2.5 MHz at 150 s
117 and descends to around 1.2 MHz by 300 s, and a lower-frequency cutoff which is at 750
118 kHz at 200 s, 200 kHz at 400 s, and remains reasonably well-defined through most of the
119 flight. This lower-frequency cutoff is interpreted as f_{pe} , which is an upper bound for the
120 whistler mode during the portion of the flight when $f_{pe} < f_{ce}$, approximately 190 to 900 s.
121 The upper cutoff is identified as the upper-hybrid frequency $f_{uh} = \sqrt{f_{pe}^2 + f_{ce}^2}$, given that
122 f_{ce} is approximately 1.2 MHz throughout the flight. The relation between the frequencies
123 of these cutoffs when they occur together lends confidence to their interpretations as f_{pe}
124 and f_{ce} .

125 The second half of the flight includes lengthy periods of intense wave activity near the
126 f_{pe} cutoff, and close inspection of waveforms shows that these consist of many bursts of
127 Langmuir waves. *LaBelle et al.* [2010] investigated 41 bursts occurring during the 850–
128 861 s interval. They estimated that over 1000 bursts occurred over the entire flight, with
129 durations from 20 to 250 ms, amplitudes ranging from a few mV/m to nearly 1 V/m, and
130 with modulation frequencies ranging from less than 1 kHz to over 50 kHz.

131 The period from 690 to 780 s, outlined in white in Figure 2a, showed strong activity
132 on both HF electric-field instruments. This period is expanded in Figure 2b for the HFE,
133 and Figure 2c from the TAEFWD Z' channel. This channel (and its counterpart Y')
134 is a composite channel derived by taking a linear combination of the real TAEFWD Y
135 and Z channels, such that Z' is parallel to the spin axis (and thus the HFE boom), and
136 Y' is orthogonal to Z' and X . The TAEFWD is somewhat less sensitive than the HFE,
137 and suffers from some instrumental interference which produces the horizontal bands in
138 Figure 2c. Nevertheless, after eliminating weak bursts which were dominated by interfer-
139 ence or showed no clear modulation, approximately 50 clean TAEFWD snapshots with
140 examples of bursty Langmuir waves were identified in this time period.

141 Figure 3 shows four selected 3-channel, 2048-sample, 0.256 ms TAEFWD snapshots
142 corresponding to the times indicated by arrows in Figure 2c. In each example, the top,
143 middle, and bottom panels show the X , Y' , and Z' components of the HF electric field,
144 respectively. In all of the waveforms in Figure 3, interference appears as discontinuous
145 pulses at approximately $25 \mu\text{s}$ intervals; however, for the selected snapshots, the wave am-
146 plitude is high enough that these interference spikes do not affect identification of peaks
147 and nulls in the wave modulation. All channels were normalized such that the Z' compo-
148 nent derived from TAEFWD data was equal in magnitude to the axial component of the
149 HF electric field derived from HFE data, which was in turn converted to absolute electric-
150 field units using pre-launch HFE calibrations, with an adjustment factor to account for
151 probe-plasma sheath capacitance.

152 Figure 3a shows waveforms from within a typical burst of cusp Langmuir waves, occur-
153 ring at 699.8523 s. The variations in amplitude represent the Langmuir wave modulation

154 which has been studied by many authors [*Bonnell et al.*, 1997; *Stasiewicz et al.*, 1996;
155 *LaBelle et al.*, 2010]. The typical modulation frequency is 10 kHz, or 0.1 ms, so the
156 0.256 ms duration TAEFWD snapshots catch only a small portion of the total modu-
157 lated wave burst, implying that these plots show only one or a few modulation cycles
158 out of many that occurred. In this example, the modulation nulls about 30 μ s from the
159 start of the snapshot are synchronous across all channels, i.e. the modulation of the x,
160 y, and z components of the electric field are in-phase, and the burst modulation is rela-
161 tively low-frequency (~ 15 kHz) and approximately monochromatic, implying sinusoidal
162 modulation. Figure 3b from 768.0764 s shows an example with faster, multi-frequency
163 modulation. This results in multiple nulls and peaks, which are variably spaced in time.
164 As in the first example, the modulation is isotropic, i.e. in-phase on the three components
165 of the wave electric field.

166 Of the snapshots with clear, high-powered bursts, up to 25% show modulation that
167 appears to be anisotropic, i.e., the modulation nulls and peaks are not synchronous in
168 the three electric-field components. Figure 3c from 715.2763 s shows an example of this
169 behavior, with the modulation nulls and peaks coming at different times in different chan-
170 nels: e.g. a null appears in the X component at 715.276375 s, then in the Y' component 20
171 μ s later, and finally in the Z' component after another 20 μ s. In this case, the modulation
172 appears similar in the three electric field components, but peaks and nulls are delayed.
173 In other cases, the modulation of the wave electric field components is not only asyn-
174 chronous, but the modulation appears entirely uncorrelated. Figure 3d shows an example
175 of this behavior, from 739.0204 s. Starting from 739.02000 s, the nulls in this snapshot
176 appear at 45 μ s, 49.5 μ s, 48.5 μ s, and 58 μ s in the X component, while the only clear

177 nulls in the Y' component are at $39.5 \mu\text{s}$ and $52.5 \mu\text{s}$, and the Z' component shows no
178 clear nulls.

4. Wave Beating and Polarization

179 These first three-dimensional Langmuir-wave observations from a rocket show that, up
180 to 25% of the time, the modulation of bursty Langmuir waves is anisotropic, meaning
181 that the nulls and peaks are out of phase in the three electric field components. The
182 superposition of two or more linearly polarized waves cannot produce such an effect. We
183 postulate that the anisotropic modulations observed in TRICE high-flyer TAEFWD data
184 result from mixing of Langmuir/whistler-mode waves with a variety of polarizations. To
185 test the plausibility of this postulate, we model the superposition of combinations of
186 wave normal modes which occur in a plasma similar to that encountered by the TRICE
187 high-flyer from 690 to 780 s.

188 Figure 4 shows the result of numerical calculations of wave dispersion characteristics
189 for high-frequency waves in the ionosphere. This dispersion surface was calculated using
190 J-WHAMP, a Java-enhanced version of the Waves in Homogeneous Anisotropic Multi-
191 component Plasmas (WHAMP) program developed by *Rönmark* [1982]. This code uses
192 numerical approximations of linear Vlasov theory to map out dispersion relations for a
193 given set of plasma and environmental parameters, returning the basic characteristics of
194 the normal modes, such as frequency (ω), wavenumber parallel to the ambient magnetic
195 field (k_{\parallel}), and wavenumber perpendicular to B (k_{\perp}). It also returns many additional
196 plasma, wave, and field characteristics, such as Alfvén speed, polarization, Stokes param-
197 eters, etc.

198 The plotted surface in Figure 4 is the locus of frequencies and wave vectors corresponding
 199 to the normal modes of the plasma. The x and y axes represent the logarithm of k_{\perp} and
 200 k_{\parallel} , respectively, with each normalized to the electron gyroradius ρ_e . The vertical axis
 201 shows ω at a given $(k_{\perp}, k_{\parallel})$, normalized to the electron cyclotron frequency. The dashed
 202 line shows a constant-frequency contour, just below f_{pe} . The parameters used to generate
 203 this surface were selected to match plasma conditions encountered by the TRICE high-
 204 flyer during the 690 to 780 s period: $B_0 = 36.850 \mu\text{T}$ (implying $f_{ce} = 1031.800 \text{ kHz}$),
 205 and a single particle species set for electron parameters, with $n = 2149 \text{ cm}^{-3}$ (implying
 206 $f_{pe} = 417 \text{ kHz}$) and an isotropic temperature of 2 eV with no loss cone. The model plasma
 207 includes only thermal (background ionosphere) electrons, because this population is what
 208 determines the real part of the wave dispersion relation, i.e. the frequencies, wave vectors,
 209 and polarization of the normal modes. At these frequencies, ions are a static background,
 210 with no significant effect. A more-complex electron beam model would be required to
 211 calculate the imaginary part of the dispersion relation (e.g. to examine damping rates),
 212 but is not required for our investigation of interference as a function of wave polarization,
 213 as an unrealistically high-density beam would be required to affect the mode structure and
 214 polarization. In the aurora, beam densities are typically 10^{-3} smaller than the ambient
 215 electron density. The significant J-WHAMP outputs for this analysis are those related to
 216 the polarization of normal modes: electric-field coefficients for generated waves, and the
 217 ellipticity parameter, which is a measure of polarization ranging from -1 (left-circularly
 218 polarized) through 0 (linearly polarized) to +1 (right-circularly polarized). In Figure 4,
 219 the ellipticity is represented by the color of the dispersion surface.

220 The dispersion characteristics of Figure 4 are similar to those calculated by *André*
 221 [1985], specifically his ‘model 2’ for an $f_{pe} < f_{ce}$ regime. In the limit $k_{\parallel} \gtrsim k_{\perp}$ and $k_{\parallel}\rho_e \gg$
 222 0.001, the surface corresponds to Langmuir waves, for which $\omega \approx \omega_{pe}$ at intermediate k .
 223 Dispersion sets in at short wavelengths ($k_{\parallel}\rho_e > 0.1$) due to finite electron temperature
 224 effects. For $k_{\parallel} \gg k_{\perp}$ and long wavelengths in the $f_{pe} < f_{ce}$ regime, the Langmuir mode
 225 smoothly couples to the whistler mode, and the surface is better described as ‘Langmuir-
 226 whistler modes’ [Layden et al., 2011]. These mode identifications can also be confirmed
 227 by the ellipticity: a region of strong right-elliptical polarization (REP) coincides with the
 228 whistler modes, while the Langmuir wave modes are more linearly polarized (LP).

229 The observations show modulated Langmuir waves which have been interpreted as wave
 230 beating due to the presence of multiple normal modes with closely spaced frequencies, e.g.
 231 waves near the 500 kHz plasma frequency with frequency separations of approximately
 232 10 kHz. To investigate the intermodulation of such closely spaced normal modes, we can
 233 select normal modes from the Figure 4 data: one on a specific frequency contour and
 234 one near that contour (though not necessarily near the first point), representing waves
 235 with relatively similar frequencies. As shown by the dashed line in Figure 4, two modes
 236 thus selected can have very close frequencies, but significantly different wave vectors and
 237 polarizations. For example, one wave can be partway down the whistler dispersion curve,
 238 in the range of REP wave modes, and the other can lie in the mostly LP Langmuir wave
 239 region.

240 In order to simulate the superposition of two waves, we start by extracting five
 241 parameters— k_{\perp} , k_{\parallel} , and the complex E_x , E_y , and E_z coefficients—from the J-WHAMP
 242 output, for two selected normal modes from our dispersion surface. The E coefficients

output by J-WHAMP are normalized such that $|E| = 1$ mV/m, thus assuring that the interacting waves have comparable amplitudes, and modulation peaks and nulls should be at their most-pronounced. The parameters are plugged into the general plane wave equation summed over both waves

$$\vec{E}(t) = \begin{cases} \left(E_{x1}e^{-i(k_1 \cdot \vec{x} - \omega t)} + E_{x2}e^{-i(k_2 \cdot \vec{x} - \omega t)} \right) \hat{x} + \\ \left(E_{y1}e^{-i(k_1 \cdot \vec{x} - \omega t)} + E_{y2}e^{-i(k_2 \cdot \vec{x} - \omega t)} \right) \hat{y} + \\ \left(E_{z1}e^{-i(k_1 \cdot \vec{x} - \omega t)} + E_{z2}e^{-i(k_2 \cdot \vec{x} - \omega t)} \right) \hat{z} \end{cases} .$$

There exists an ambiguity in any dispersion solution which results in a rotational freedom around the k_{\parallel} axis. J-WHAMP defines that $k_{\parallel} \equiv k_z$ and $k_{\perp} \equiv k_x$, implying that k_y must be zero—this is not a fully general solution. Appendix A examines this k_{\perp} ambiguity with respect to J-WHAMP output, and finds that rotations around the z axis can generate some beat modulation anisotropy, but cannot fully explain the observations. Furthermore, in order to optimally pick up beating between the x and y components of waves, one must rotate all beating waves by an angle $\phi = 45$ degrees around the z axis. Figure 5 shows the results of the simulations, for four pairs of normal modes from the Langmuir plane, with $\phi = 45$ degrees. Using J-WHAMP definitions of the coordinates, the x , y , and z directions roughly correspond to those in the TAEFWD data, with z parallel to B_0 , and x and y perpendicular. Table 1 lists the full parameters (f_{pe} , E , k , and ψ) used for the Figure 5 simulations.

Figure 5a shows the result of combining two simulated wave modes from the LP Langmuir dispersion region, at sufficiently short wavelengths for $\omega \sim \omega_{pe}$. As expected, the resulting modulation occurs with a 330 μ s period ($1/\Delta f \Rightarrow 1/(3$ kHz)). In this case, corresponding to beating of two LP waves, the wave modulation is isotropic, i.e. maxima and minima coincide in time, similar to the observations shown in Figures 3a and b. Figure 5b shows the similar wave modulation that results from superposing two REP waves

265 selected from the region $k_{\parallel} \sim 0.001$ and $k_{\perp} < 0.001$, which is within the whistler-mode
 266 part of the dispersion surface. The resulting modulation has a 660 μs period, and shows
 267 isotropic modulation.

268 In Figure 5c and d, the wave modes pairs from a and b were combined to make two
 269 mixed pairs in order to investigate beating between waves of different polarizations. This
 270 combination of one wave mode from each dispersion region yields modulation anisotropy,
 271 such that the nulls in each component occur at different times. In Figure 5c, the null in
 272 the x component is delayed 100 μs from the null in z, and 200 μs from the null in y. This
 273 is qualitatively and quantitatively similar to the effect observed in Figure 3c.

274 A close examination of power spectra of the four waveform snapshots shown in Fig-
 275 ure 3 lends some support to this interpretation; however, for TRICE TAEFWD data, the
 276 frequency resolution of the spectra is limited due to the short duration of the waveform
 277 snapshots. Figure 6 shows power spectra with the horizontal axis zoomed in to a narrow
 278 range of frequencies centered around f_{pe} for a given snapshot. The dashed, black line
 279 shows power in the (Z') component, which is roughly parallel to B_0 , while the red line
 280 shows ‘perpendicular power’, which is the sum of the power in the X and Y' components.
 281 As expected, more power is generally found in the parallel direction, but anywhere from
 282 5% to 50% of the power near f_{pe} can be found in the perpendicular direction, depend-
 283 ing on snapshot. This implies that a significant fraction of the waves present lie in the
 284 oblique regions of k -space (i.e. away from the x and y axes in Figure 4), which implies
 285 that multiple wave modes with different polarizations may be present.

286 A method of spectral analysis of polarization is taken from *LaBelle and Treumann*
 287 [1992], adapted from *Kodera et al.* [1977]. Given time series data corresponding to two

perpendicular, transverse components of the wave electric field, as from the measured X
 and reconstructed Y' components from the TAEFWD, a spectral power can be estimated
 for left- and right-polarized waves by recombining the complex Fast Fourier Transforms
 (FFT) of the time series, according to

$$\begin{aligned} FFT_L &= FFT_X + \mathbf{i} FFT_Y, \\ \text{and } FFT_R &= FFT_X - \mathbf{i} FFT_Y. \end{aligned}$$

The relative power ratio $|FFT_L|^2/|FFT_R|^2$ indicates whether the waves at a given frequency are predominately left, right, or linearly polarized. Figure 7 shows the results of this analysis, again zoomed in near f_{pe} . While the small number of samples in each snapshot limit frequency resolution such that the individual peaks for the beating waves are not resolved, the variations seen in these spectra suggest that mixing of linear and elliptically-polarized waves is occurring to some degree.

5. Conclusion

An analysis of a period of strong Langmuir waves observed in cusp aurora by two HF electric field instruments on the TRICE high-flyer sounding rocket shows many examples of Langmuir wave bursts modulated at approximately 10 kHz. Previous studies have explained these observations as the result of beating between waves with very close frequencies near the Langmuir cutoff.

The unique 3-D data set provided by the NASA GSFC TAEFWD instrument shows that up to 25% of waveforms selected from the most-intense bursts exhibit anisotropic modulations, i.e. the beat nulls and peaks are not aligned in time across the three perpendicular electric field components. Anisotropic modulation can arise when superposed wave normal modes possess differing polarizations, e.g. if a more linearly-polarized Langmuir wave

308 mixes with a right-elliptically-polarized whistler wave. The J-WHAMP numerical disper-
 309 sion code shows that conditions appropriate to the observations can produce such waves,
 310 and simulations of such superpositions show that they do produce anisotropic modula-
 311 tion. Analysis of wavevector ambiguities (Appendix A) implies that the orientation of
 312 the beating waves with respect to each other and to the instrument probes cannot fully
 313 explain the observed effect, though they can mask it. FFT analysis of the 3-D waveform
 314 data, though limited due to the short duration of waveform snapshots, suggests that both
 315 linear and elliptically-polarized waves are present near the Langmuir cutoff at these times.
 316 Because either proposed origin of the beating waves could produce waves with multiple
 317 polarizations, these findings do not resolve the origin of the multiple modes. Neverthe-
 318 less, these observations illustrate how 3-D measurements can give valuable insight into the
 319 nature of wave interactions in the auroral plasma environment, and suggest that future
 320 measurements should have a higher duty cycle, and perhaps even be continuous.

Appendix A: The k_{\perp} Ambiguity

321 The background magnetic field provides a natural axis in a plasma environment, which
 322 motivates a k_{\parallel} and k_{\perp} coordinate system, but with rotational freedom around k_{\parallel} ; i.e., k_{\perp}
 323 can lie anywhere in a plane perpendicular to the background magnetic field. J-WHAMP
 324 resolves this ambiguity by defining k_{\parallel} to be along the z axis, k_{\perp} to be along the x axis, and
 325 $k_y = 0$. While \vec{k} does not directly affect the simulations because of the simplification that
 326 $\vec{x} = \vec{0}$, information on the wave's orientation will be a part of the complex \vec{E}_0 , and so a
 327 more general simulation will have $k_x \neq k_y \neq 0$. One can simulate such a state by rotating
 328 one of the component waves in the beat simulations around \hat{z} . Looking at a general \hat{z}
 329 rotation by an angle ϕ , and assuming $\vec{E}_0 \in \mathbb{R}$ so that a 100% right-circularly-polarized

wave will have components $(E_x, \mathbf{i}E_y, E_z)$,

$$\begin{pmatrix} \cos \phi & -\sin \phi & 0 \\ \sin \phi & \cos \phi & 0 \\ 0 & 0 & 1 \end{pmatrix} \begin{pmatrix} E_x \\ \mathbf{i}E_y \\ E_z \end{pmatrix} = \begin{pmatrix} E_x \cos \phi - \mathbf{i}E_y \sin \phi \\ E_x \sin \phi + \mathbf{i}E_y \cos \phi \\ E_z \end{pmatrix}.$$

Through judicious use of Euler identities, this can be manipulated into the form

$$\begin{pmatrix} \mathbf{e}^{\mathbf{i}\phi} \cdot f(E_x, E_y, \phi) \\ \mathbf{e}^{\mathbf{i}\phi} \cdot g(E_x, E_y, \phi) \\ E_z \end{pmatrix} \Big| (f, g) \in \mathbb{C}.$$

This shows that the rotation can be broken down into complex ϕ -dependent amplitudes times an equal phase shift of the x and y components with respect to z . The fact that the x and y modulation phases remain synchronous would imply that not all of the modulation phase anisotropy seen in TAEFWD data can be explained simply by the beating waves having different wavevectors. In Figure 8 this is confirmed in simulation, showing the change in beat patterns while rotating one of the component waves. While there is some small shift in the x - y phase alignment, it is insufficient to reproduce, for example, Figure 3c, and can probably be attributed to the small difference in ellipticity between the two chosen wave modes.

An additional effect of the J-WHAMP alignment of k_{\perp} arises because the axes in ‘WHAMP-space’ are effectively probes in the simulated plasma environment. With the axes aligned with the waves as output by J-WHAMP, the effect is such that any beating caused by interaction between E_x and E_y cannot be seen, as in Figure 9 where no modulation is seen in the y component, which is qualitatively similar to the lack of modulation in the z component of Figure 3d. As depicted in Figure 9, testing of various amounts of rotation of all beating component waves around the z axis by an angle ψ (effectively rotating the ‘virtual payload’ used to ‘detect’ k and \vec{E}), yields the conclusion that the payload orientation can have a significant impact on how well any modulation will be

350 detected, and that $\psi = 45$ degrees is the optimal angle to detect beating in our simula-
351 tions. It is possible that the physical version of such effects may be seen in the TAEFWD
352 observations, in cases where strong modulations are seen in only two of three directions,
353 e.g. Figure 3d.

References

- 354 André, M., Dispersion surfaces, *Journal of Plasma Physics*, *33*(01), 1–19, doi:
355 10.1017/S0022377800002270, 1985.
- 356 Beghin, C., J. L. Rauch, and J. M. Bosqued, Electrostatic plasma waves and hf auroral
357 hiss generated at low altitude, *J. Geophys. Res.*, *94*(A2), 1359–1378, 1981.
- 358 Boehm, M. H., Waves and static electric fields in the auroral acceleration region, Ph.D.
359 thesis, University of California, Berkeley, 1987.
- 360 Bonnell, J., P. Kintner, J. E. Wahlund, and J. A. Holtet, Modulated langmuir waves:
361 Observations from freja and scifer, *J. Geophys. Res.*, *102*(A8), 1997.
- 362 Ergun, R. E., C. W. Carlson, J. P. McFadden, J. H. Clemmons, and M. H. Boehm,
363 Evidence of a transverse langmuir modulational instability in a space plasma, *Geophys.*
364 *Res. Lett.*, *18*, 1177, 1991.
- 365 Kaeppler, S., et al., Current closure in the auroral ionosphere: Results from the auroral
366 current and electrodynamics structure rocket mission, submitted Nov 2011, 2011.
- 367 Khotyaintsev, Y., G. Lizunov, and K. Stasiewicz, Langmuir wave structures registered by
368 freja: Analysis and modeling, *Adv. Space Res.*, *28*, 1649, 2001.
- 369 Kintner, P. M., et al., The scifer experiment, *J. Geophys. Res.*, *101*, 1865, 1996.

- 370 Kletzing, C. A., J. LaBelle, D. E. Rowland, R. F. Pfaff, S. Kaeppler, and M. P. Dom-
371 browski, Untitled, in process paper on CHARM II WPI data, 2012.
- 372 Kodera, K., R. Gendrin, and C. de Villedary, Complex representation of a polarized signal
373 and its application to the analysis of ulf waves, *J. Geophys. Res.*, *82*(7), 1245–1255,
374 1977.
- 375 LaBelle, J., and R. A. Treumann, Poynting vector measurements of electromagnetic ion
376 cyclotron waves in the plasmasphere, *J. Geophys. Res.*, *97* (A9)(13), 789–797, 1992.
- 377 LaBelle, J. W., I. H. Cairns, and C. A. Kletzing, Electric field statistics and modula-
378 tion characteristics of bursty langmuir waves observed in the cusp, *J. Geophys. Res.*,
379 *115*(A1), 317, 2010.
- 380 Layden, A., I. H. Cairns, P. Robinson, and J. LaBelle, Changes in mode properties versus
381 mode conversion for waves in earth’s auroral ionosphere, *J. Geophys. Res.*, *116*(A12328),
382 2011.
- 383 Lizunov, G. V., Y. Khotyaintsev, and K. Stasiewicz, Parametric decay to lower hybrid
384 waves as a source of modulated langmuir waves in the topside ionosphere, *J. Geophys.*
385 *Res.*, *106*, 24,755, 2001.
- 386 Maggs, J. E., Coherent generation of vlf hiss, *J. Geophys. Res.*, *81*, 1707, 1976.
- 387 McAdams, K. L., J. LaBelle, P. W. Schuck, and P. M. Kintner, Phaze ii observations
388 of lower hybrid burst structures occurring on density gradients, *Geophys. Res. Lett.*,
389 *25*(16), 3091–3094, 1998.
- 390 McAdams, K. L., J. LaBelle, and M. L. Trimpi, Rocket observations of banded struc-
391 ture in waves near the langmuir frequency in the auroral ionosphere, *J. Geophys. Res.*,
392 *104*(A12), 28,109–28,122, 1999.

- 393 McFadden, J. P., C. W. Carlson, and M. H. Boehm, High-frequency waves generated by
394 auroral electrons, *J. Geophys. Res.*, *91*, 12,079, 1986.
- 395 Newman, D., M. Goldman, and R. E. Ergun, Langmuir turbulence in the auroral iono-
396 sphere, 2. nonlinear theory and simulations, *J. Geophys. Res.*, *99*, 6377, 1994a.
- 397 Newman, D., M. Goldman, R. E. Ergun, and M. H. Boehm, Langmuir turbulence in the
398 auroral ionosphere, 1. linear theory, *J. Geophys. Res.*, *99*, 6367, 1994b.
- 399 Rönnmark, K., Whamp- waves in homogeneous, anisotropic multicomponent plasmas,
400 *Tech. Rep. 179*, Kiruna Geophysical Institute, 1982.
- 401 Samara, M., and J. LaBelle, Lf/mf whistler mode dispersive signals observed with
402 rocket-borne instruments in the auroral downward current region, *J. Geophys. Res.*,
403 *111*(A09305), 2006.
- 404 Samara, M., J. LaBelle, C. A. Kletzing, and S. R. Bounds, Rocket observations of struc-
405 tured upper hybrid waves at $f_{uh} = 2f_{ce}$, *Geophys. Res. Lett.*, *31*(22), 2004.
- 406 Stasiewicz, K., B. Holback, V. Krasnoselskikh, M. H. Boehm, R. Boström, and P. M.
407 Kintner, Parametric instabilities of langmuir waves observed by freja, *J. Geophys. Res.*,
408 *101*(21), 515, 1996.

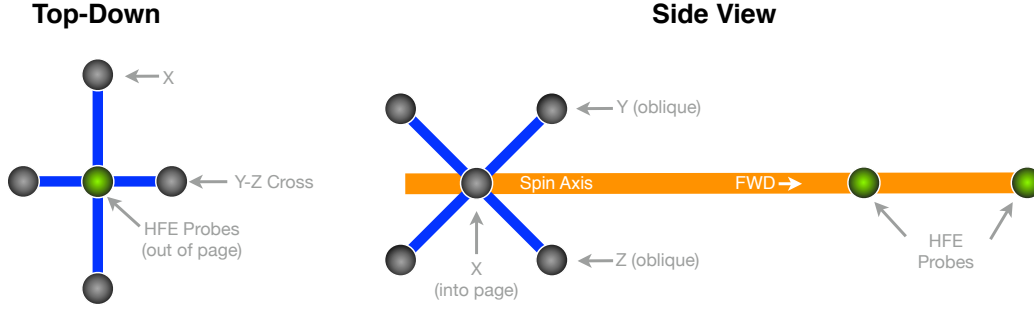


Figure 1. Boom and sensor elements of the two complimentary HF electric field experiments flown on the TRICE sounding rockets.

Table 1. Wave normal mode parameters determined from J-WHAMP and used for the waveform simulations shown in Figure 5, along with the ellipticity for each mode. Model c uses the first waves from model a and model b, and models c and d differ only in the coordinate system rotation parameter ψ .

#	ψ (deg)	LP /REP	f_{pe}/f_{ce}	$E(x, y, z)$	$k(x/\perp, y, z/\parallel)$	Ellip
a	45	LP	0.369469	(0.376424, 0.002857i, 0.926443)	(0.003162, 0, 0.007943)	0.3759
		LP	0.366606	(0.391707, 0.003042i, 0.920085)	(0.003236, 0, 0.007762)	0.3732
b	45	REP	0.368377	(0.630643, 0.512265i, 0.582988)	(0.000158, 0, 0.001380)	0.9093
		REP	0.369478	(0.632961, 0.524797i, 0.569165)	(0.000148, 0, 0.001380)	0.9176
c	45	LP	0.369469	(0.376424, 0.002857i, 0.926443)	(0.003162, 0, 0.007943)	0.3759
		REP	0.368377	(0.630642, 0.512265i, 0.582988)	(0.000158, 0, 0.001380)	0.9093
d	45	LP	0.366606	(0.391707, 0.003042i, 0.920085)	(0.003236, 0, 0.007762)	0.3732
		REP	0.369478	(0.632961, 0.524797i, 0.569165)	(0.000148, 0, 0.001380)	0.9176

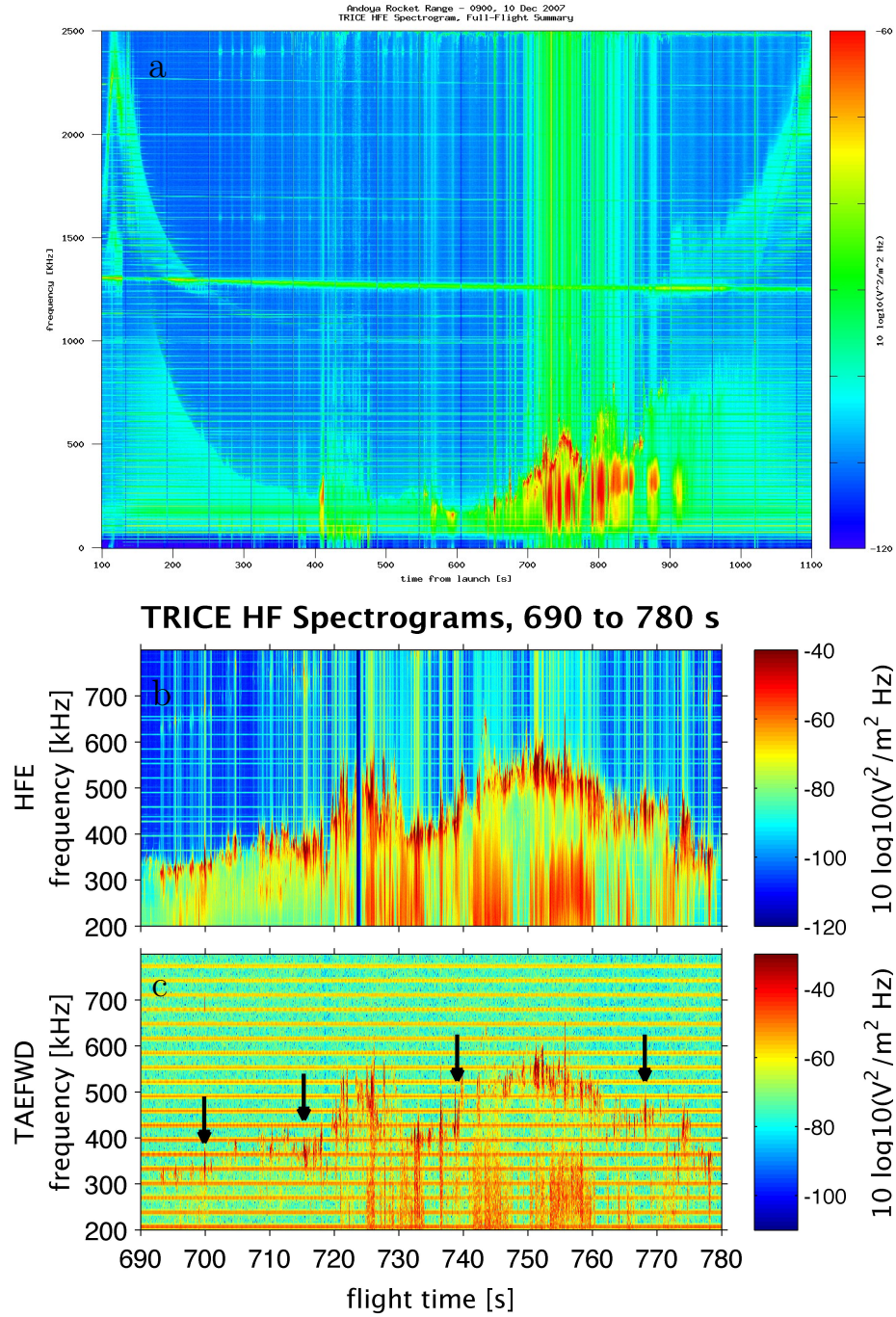


Figure 2. Spectrograms of TRICE HF electric field data. **a** shows a summary of the full flight covering 100 kHz–2.5 MHz and 100–1100 s, while **b** and **c** are HFE and TAEFWD Z' data covering a 200–800 kHz band from 690 to 780 s, the period of intense activity outlined in white in **a**. Black arrows in **c** indicate times of TAEFWD waveform snapshots examined in detail.

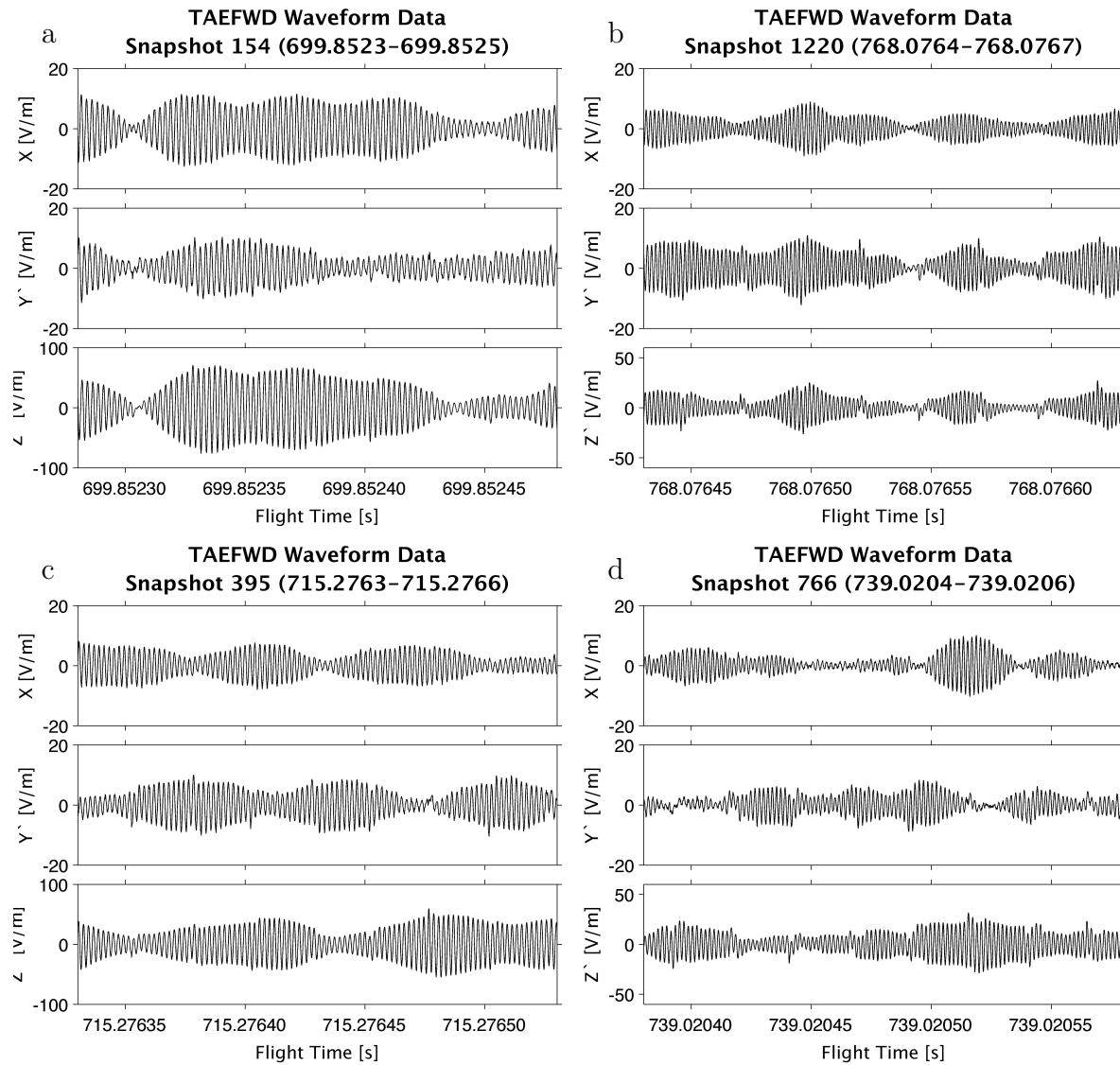


Figure 3. Waveform snapshots measured by the TAEFWD, for the four example Langmuir wave bursts indicated by arrows in Figure 2c. In **a** and **b**, the modulations of the mutually orthogonal components of wave electric field are synchronous. In **c** and **d** the modulation are not synchronous, indicating anisotropy.

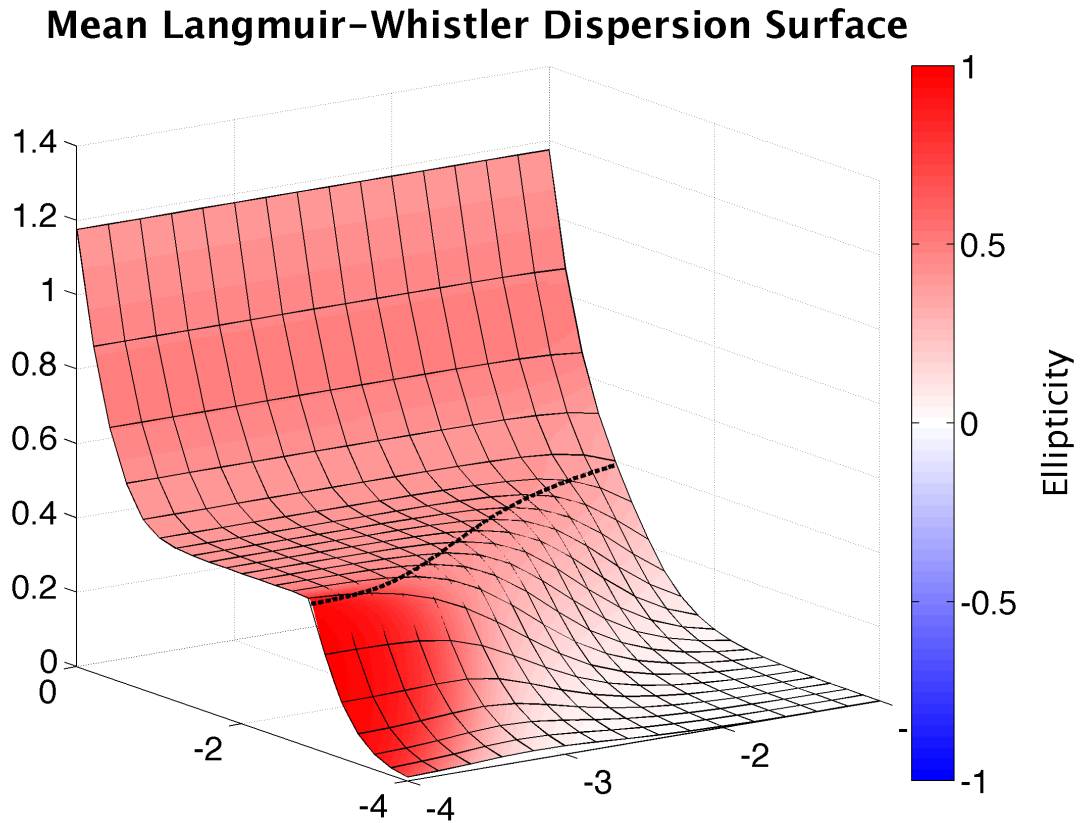


Figure 4. A dispersion relation for Langmuir and whistler waves in a homogeneous, magnetized plasma, calculated using the J-WHAMP numerical code. The surface shows frequency normalized to ω_{ce} vs. parallel and perpendicular wavevector (log scales). The model plasma approximately matches the conditions encountered by the TRICE high-flyer from 690 to 780 s. Shading of the surface represents the ellipticity of the modes, which range from left elliptically polarized (blue, not present on this surface) through linear (white) to right elliptically polarized (red). The dashed line is an example contour of constant frequency.

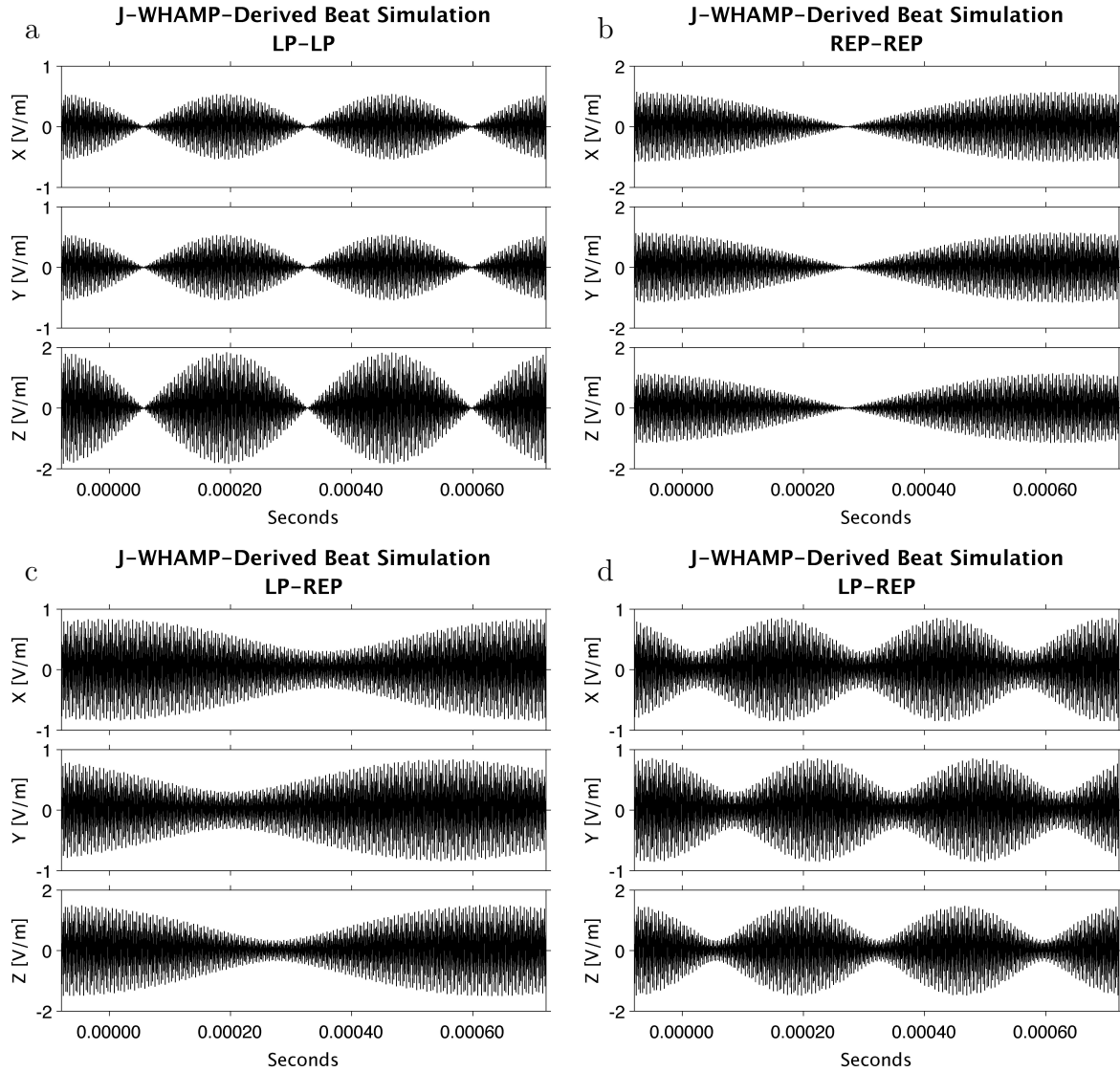


Figure 5. Simulations of beating between pairs of waves corresponding to Langmuir-whistler modes calculated with J-WHAMP. In **a** and **b** the simulated beating wave modes have the same polarization, both linearly polarized (**a**) or both right-elliptically polarized (**b**). In **c** and **d** one wave mode is used from the set in **a**, and one from **b**, so the simulated waves have different polarizations, one more-linear, one more-elliptical. **a** and **b** result in isotropic modulation of the three field components, whereas **c** and **d** result in anisotropies. Note that all waves have been rotated through 45 degrees so that J-WHAMP-calculated mode beating will be optimally detected (see Appendix).

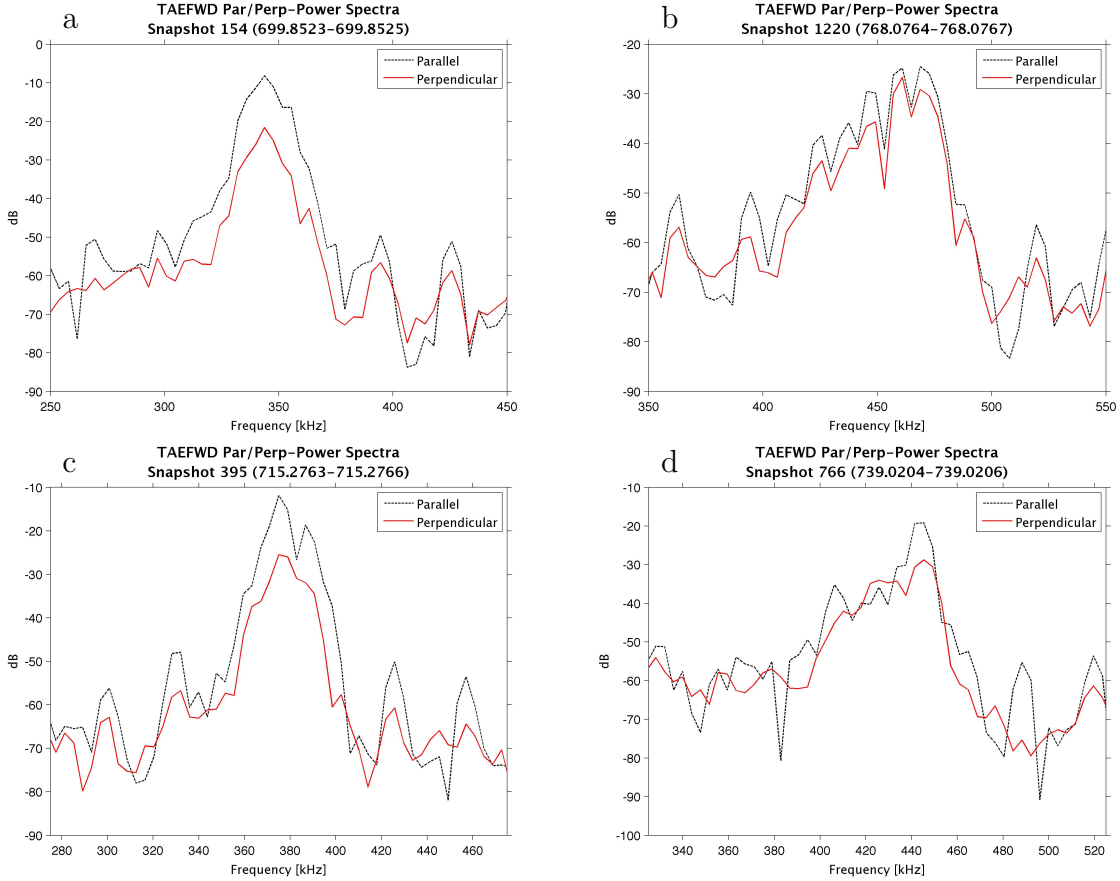


Figure 6. Power spectra of the TAEFWD waveform snapshots shown in Figure 3, showing power in the parallel (Z') and perpendicular ($X + Y'$) components. The horizontal axis shows a 200 kHz band centered on f_{pe} for the given snapshot. The significant power in the perpendicular direction implies that wave modes from a wide region of k -space are present.

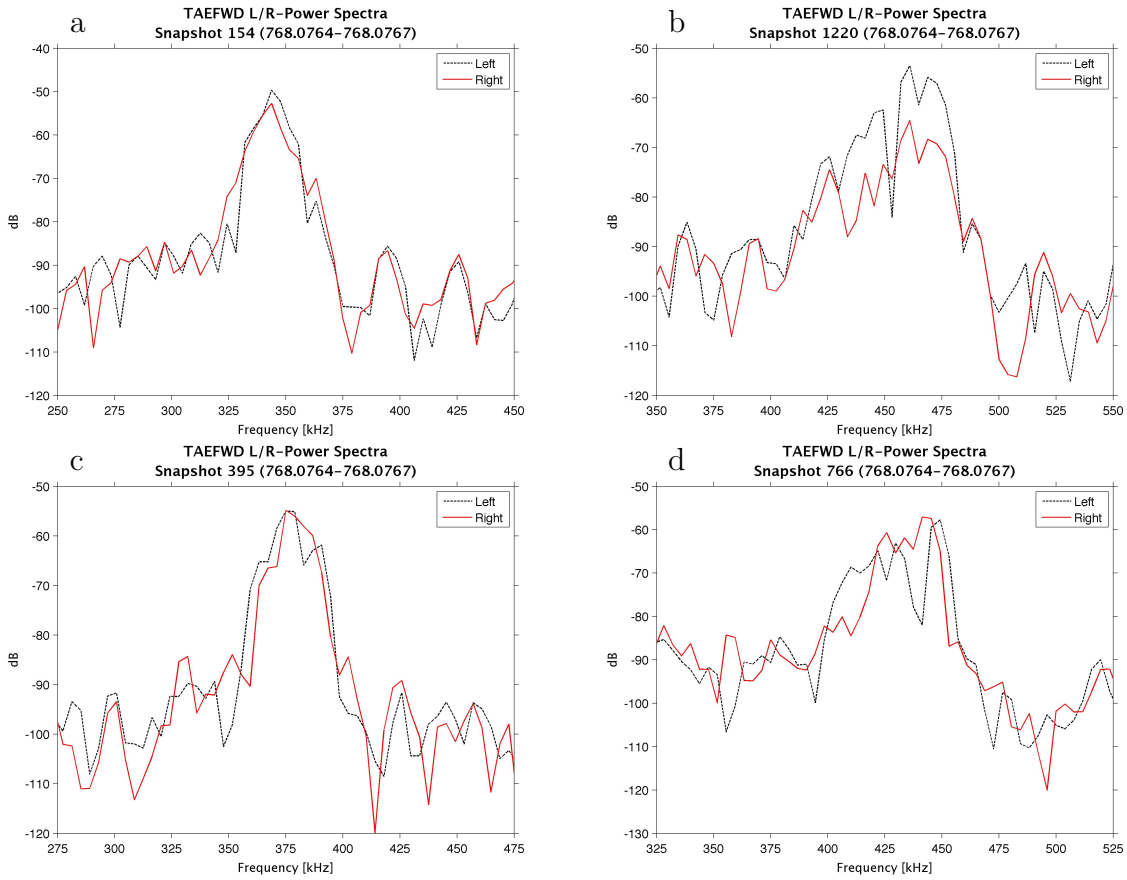


Figure 7. Power spectra of the TAEFWD waveform snapshots shown in Figure 3, with complex Fourier transforms of the transverse components (X and Y') recombined to estimate the degree of right and left circular polarization, as done in *Kodera et al.* [1977] and *LaBelle et al.* [2010]. The horizontal axis shows a 200 kHz band centered on f_{pe} for the given snapshot. While the snapshots are too short to resolve the mode composition in detail, **b**, **c**, and **d** show hints that both linear and elliptical polarizations contribute to the wave modes measured near the Langmuir frequency.

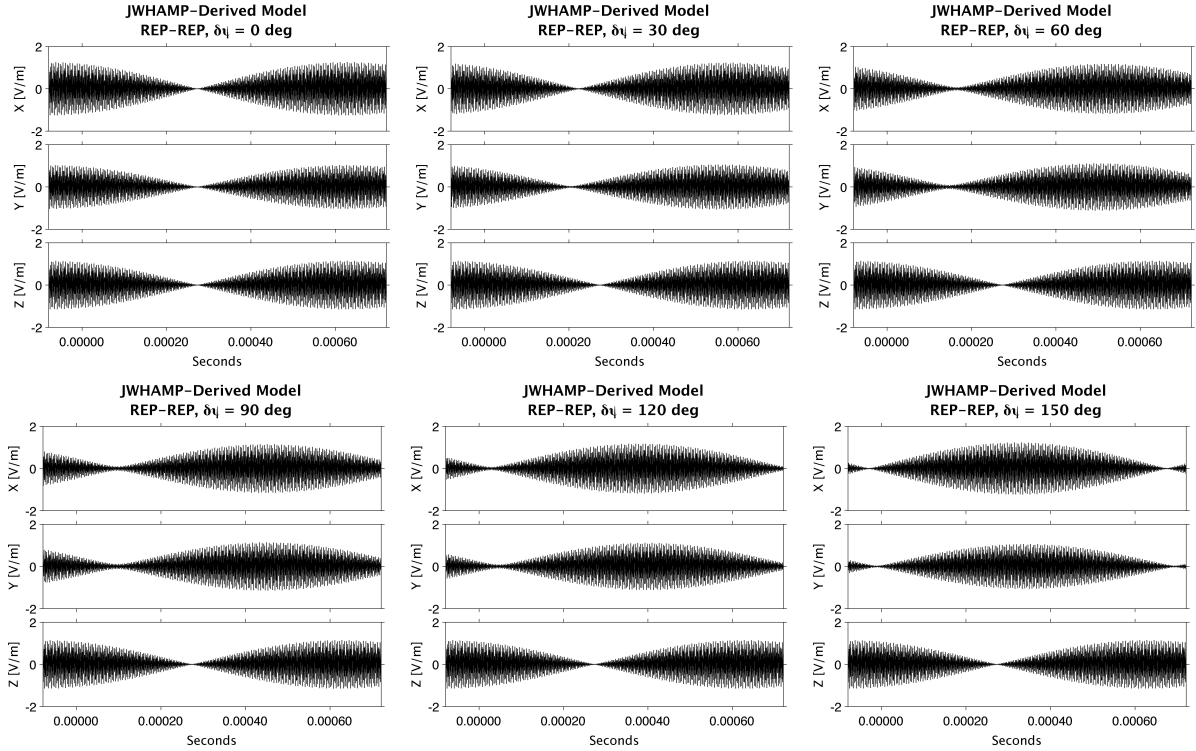


Figure 8. Simulation of two beating, mostly-circularly polarized waves, with one held constant and the other rotated through angle ϕ around the z axis. Note that the x and y modulation phases remain mostly aligned.

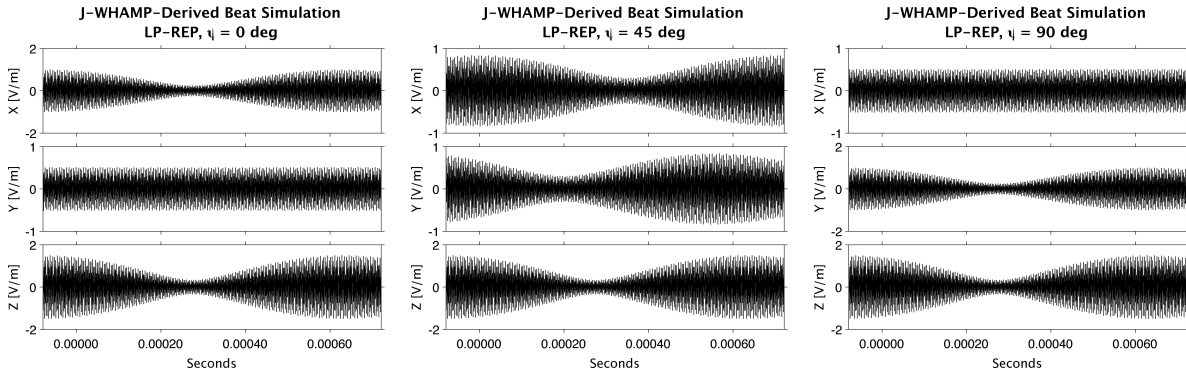


Figure 9. Results of rotating the simulation coordinate system through various angles ψ around the z axis, which is essentially the same as changing the orientation of the virtual rocket probes. The original orientation with $\psi = 0$ is entirely insensitive to beating in the y direction. Rotation through $\psi = 90$ degrees causes this insensitivity to move to the x direction, as one would expect with perpendicular axes. Strong beating in all channels with anisotropic modulation phase can be seen with $\psi = 45$ degrees.